Room temperature spin-orbit torque efficiency and magnetization switching in $SrRuO_3$-based heterostructures

Sheng Li,[1,2,3,*] Bin Lao,[1,2,*] Zengxing Lu,[1,2,*] Xuan Zheng,[1,2,4] Kenan Zhao,[1,2] Liguang Gong,[1,2] Tao Tang,[1,2] Keyi Wu,[1,2] Run-Wei Li,[1,2,3,†] and Zhiming Wang[1,2,3,‡]

[1]*CAS Key Laboratory of Magnetic Materials and Devices, Ningbo Institute of Materials Technology and Engineering, Chinese Academy of Sciences, Ningbo 315201, China*

[2]*Zhejiang Province Key Laboratory of Magnetic Materials and Application Technology, Ningbo Institute of Materials Technology and Engineering, Chinese Academy of Sciences, Ningbo 315201, China*

[3]*Center of Materials Science and Optoelectronics Engineering, University of Chinese Academy of Sciences, Beijing 100049, China*

[4]*New Materials Institute, University of Nottingham Ningbo China, Ningbo 315100, China*

(Received 29 August 2022; accepted 14 February 2023; published 23 February 2023)

Spin-orbit torques (SOTs) from transition metal oxides (TMOs) in conjunction with magnetic materials have recently attracted tremendous attention for realizing high-efficient spintronic devices. $SrRuO_3$ is a promising candidate among TMOs due to its large and tunable SOT efficiency as well as high conductivity and chemical stability. However, a further study for benchmarking the SOT efficiency and realizing SOT-driven magnetization switching in $SrRuO_3$ is still highly desired so far. Here, we systematically study the SOT properties of high-quality $SrRuO_3$ thin film heterostructuring with different magnetic alloys of both IMA and PMA configuration by the harmonic Hall voltage technique. Our results indicate that $SrRuO_3$ possesses pronounced SOT efficiency of about 0.2 at room temperature regardless of the magnetic alloys, which is comparable to typical heavy metals (HMs). Furthermore, we achieve SOT-driven magnetization switching with a low threshold current density of 3.8×10^{10} A/m^2, demonstrating the promising potential of $SrRuO_3$ for practical devices. By making a comprehensive comparison with HMs, our work unambiguously benchmarks the SOT properties and concludes the advantages of $SrRuO_3$, which may bring more diverse choices for SOT applications by utilizing hybrid-oxide/metal and all-oxide systems.

DOI: 10.1103/PhysRevMaterials.7.024418

I. INTRODUCTION

Current-induced spin-orbit torques (SOTs) provide an efficient way to manipulate magnetization states for the potential magnetic memory and oscillator applications. SOTs originate from charge-spin conversion with strong spin-orbit coupling (SOC), which is intensively studied in heavy-metals (HMs) over a decade due to their potentially useful SOT efficiency and low resistivity [1–4]. In addition to HMs, recently, a wide range of material systems are explored for realizing efficient SOT devices including topological materials [5–8], two-dimensional (2D) transition metal dichalcogenide [9–11], and transition metal oxides (TMOs) [12–23]. In particular, TMOs with perovskite structure attract tremendous attention due to their high SOT-efficiency [14–25] and rich electromagnetic properties [26–28] closely related to their exotic electronic properties, such as topological Dirac and Weyl semimetals [15–18,23] and spin-momentum locked nontrivial spin textures [24–28]. Furthermore, due to the intimate entanglement among multiple degrees of freedom, including charge, spin, orbit, and lattice, the electronic structure and the associated SOT efficiency can be precisely engineered in high quality TMO films at the atomic scale [29,30]. Therefore, TMOs provide a wide platform for searching and designing materials in future energy efficient and scalable multifunctional spintronics.

Among oxide materials, 4*d* $SrRuO_3$ (SRO) is an outstanding member of the perovskite family due to its low resistivity at ambient temperature, as well as high chemical and thermal stability [31,32]. These properties have been exploited as the electrodes for complex oxide heterostructures, such as Josephson junction, magnetic tunnel junctions, and capacitors [32–34]. Currently, it is recognized that SRO holds large Berry curvature and Weyl nodes, leading to lots of novel electromagnetic phenomena such as chiral anomaly induced negative magnetoresistance and anomalous Hall effect [28,35–37]. This intrinsic Berry phase of SRO, moreover, has been demonstrated to provide strong and highly tunable SOT properties [14–16]. The spin Hall conductivity as large as $9\times10^4\ \hbar/2e$ S m^{-1} [15] can be further manipulated via strain-controlled crystalline structure engineering. However, the reported spin Hall conductivity associated SOT efficiency ξ_{SOT} sometimes exhibits inconsistent magnitudes. For example, the ξ_{SOT} can differ by several times in the same SRO/Py heterostructures grown on $SrTiO_3$ substrates [16]. Thus, it is desirable to benchmark the SOT efficiency of SRO through a systematical study. Moreover, as a crucial step for realizing a SOT-driven device, current-induced magnetization switching has not been demonstrated in SRO so far.

*These authors contributed equally to this work.
†runweili@nimte.ac.cn
‡zhiming.wang@nimte.ac.cn

In this work, we systematically investigate the SOT properties at room temperature based on SRO/magnetic-alloy heterostructures with different magnetic easy axes both in plane and perpendicular to plane (IMA, PMA). To benchmark the SRO system, SOT efficiency and spin Hall conductivity of SRO are separately evaluated in both IMA and PMA configurations by harmonic Hall voltage technique. Besides, we demonstrate the SOT-induced magnetization switching in the PMA system, and the threshold current density could be one order of magnitude smaller than those in HMs. Finally, we compare the evaluated SOT properties with that of the previous reported SRO and HMs, and highlight the advantages of SRO as a spin source in oxide-metal hybrid and all-oxide systems for various SOT applications.

II. METHODS

A. Film fabrication and characterizations

Single crystal SRO films of 20 nm are deposited on the (001)-oriented $SrTiO_3$ (STO) substrates by pulsed laser deposition (PLD) with a KrF excimer laser ($\lambda = 248$ nm). During the deposition, the substrate temperature is set at 670 °C and the oxygen partial pressure is 0.1 mbar. The energy density of the laser spot is 2.45 J/cm^2. After SRO growth, the films are cooled to room temperature with a rate of 10 °C/min in 1 mbar oxygen atmosphere. To prepare the IMA sample, a 7-nm Py ($Ni_{80}Fe_{20}$) layer is deposited *in situ* on the SRO under high vacuum. After the SRO/Py deposition, a 2-nm STO capper is grown as a protective layer. For the PMA sample, a Co/Pt multilayer (referred to as CoPt) with a stacking structure of Pt(1 nm)/Co(0.5 nm)/Pt(0.5 nm)/Co(0.5 nm)/Pt(1 nm) is sputtered on bare SRO by a magnetron sputter at room temperature after a thermal treatment at 300 °C to obtain a clean surface. The thickness of SRO layer (t_{SRO}) is monitored by the *in situ* reflection high energy electron diffraction (RHEED) equipped in PLD during the growth processions, and the thicknesses of Py and CoPt layers are evaluated by x-ray reflectivity (XRR) measurement. The saturation magnetization M_S is confirmed via measuring the magnetization hysteresis loop by superconducting quantum interference device (SQUID, Quantum Design) and ferromagnetic resonance (FMR) measurement (see details in Supplemental Material S1 [38]). The magnetic anisotropy field H_k of Py is probed by the hysteresis loop and anomalous Hall effect measurement.

B. Device fabrication and measurements

For electrical measurements, the samples are fabricated into Hall bar devices using standard photolithography and argon ion etching techniques. The Hall bar pattern has channel dimension of 10 μm in current-interface width and 5 μm in voltage-interface width. After that, 10 nm Ti and 50 nm Au are successively deposited on the Hall bar pattern by electron-beam evaporation. The electrical measurements are performed on the home-built low-temperature and high magnetic field electronic test system. Various AC currents with a fixed frequency 133.73 Hz and pulsed DC currents are applied by Keithley 6221 current source, and the DC current is generated by Keithley 6220 current source. The harmonic voltage signals and DC voltage signal are respectively measured by SR830 DSP lock-in amplifiers and a Keithley 2182A nanovoltmeter.

III. RESULTS

A. SRO/Py and SRO/CoPt hybrid structures

High-quality SRO thin film with a thickness of 20 nm is epitaxially grown on (001)-orientated $SrTiO_3$ (STO) substrate by PLD. Structural properties of the film are determined by high-resolution x-ray diffraction (XRD) measurements. Figure 1(a) shows the θ-2θ scan of the SRO film, in which distinct (001) and (002) peaks of both film and substrate imply the epitaxial growth of the film. The well-defined Kiessig fringes indicate a sharp SRO/STO interface and flat surface. According to the peak position, the out-of-plane lattice constant is calculated as 3.942 Å by Bragg's law, which is larger than the bulk value 3.925 Å, indicating an in-plane compressive strain in the deposited film. Figure 1(b) exhibits the epitaxial relationship between the SRO film and substrate characterized via x-ray reciprocal space mapping (RSM) along the (103) direction, in which the identical Q_X values strongly suggest that the film is fully strained by the substrate. The atomic force microscope (AFM) result demonstrates an atomically flat surface with clear terraces and a root-mean-square roughness of about 0.12 nm, as shown in Fig. 1(c), which is consistent with the XRD results. After preparation of the SRO, two magnetic components, 7-nm Py with IMA and 3.5-nm CoPt with PMA, are individually deposited on the bare SRO by PLD and magnetron sputter, respectively. Thereafter, two different SOT-switching systems with IMA and PMA, i.e., SRO/Py and SRO/CoPt, are prepared. Their hysteresis loops measured by SQUID as shown in Figs. 1(d) and 1(e), respectively.

B. SOT efficiency of IMA system

The harmonic Hall voltage measurements are performed to characterize the SOT properties in the SRO/Py sample with IMA [11,39,40]. Figure 2(a) schematically presents the sample structure, directions of applied charge current I, and external magnetic field H in our measurement configuration. The first and second harmonic Hall voltages, $V_{xy}^{1\omega}$ and $V_{xy}^{2\omega}$, are acquired simultaneously while rotating the angle φ between H and I [41–43]. Figure 2(b) shows typical $V_{xy}^{1\omega}$ signals as a function of φ. Since the $V_{xy}^{1\omega}$ is equivalent to conventional Hall voltage, the obtained $\cos 2\varphi$ dependence indicates that the magnetization in the IMA sample is always aligned in plane during the measurements. The $V_{xy}^{2\omega}$ provides information about the spin current induced SOT, which causes a small precession of the magnetization M about its equilibrium position against external field. Correspondingly, the dampinglike and fieldlike components can be quantitatively analyzed via the $V_{xy}^{1\omega}$ and $V_{xy}^{2\omega}$ results by the following formulas:

$$V_{xy}^{1\omega} = V_{\mathrm{PHE}} \sin 2\varphi, \tag{1}$$

$$V_{xy}^{2\omega} = \tfrac{1}{2} V_{\mathrm{DL}} \cos\varphi + (-V_{\mathrm{FL}} \cos\varphi \cos 2\varphi), \tag{2}$$

$$V_{\mathrm{DL}} = \frac{V_{\mathrm{AHE}}}{H_K - H} H_{\mathrm{DL}}, \tag{3}$$

$$V_{\mathrm{FL}} = \frac{V_{\mathrm{PHE}}}{H} (H_{\mathrm{FL}} + H_{\mathrm{Oe}}). \tag{4}$$

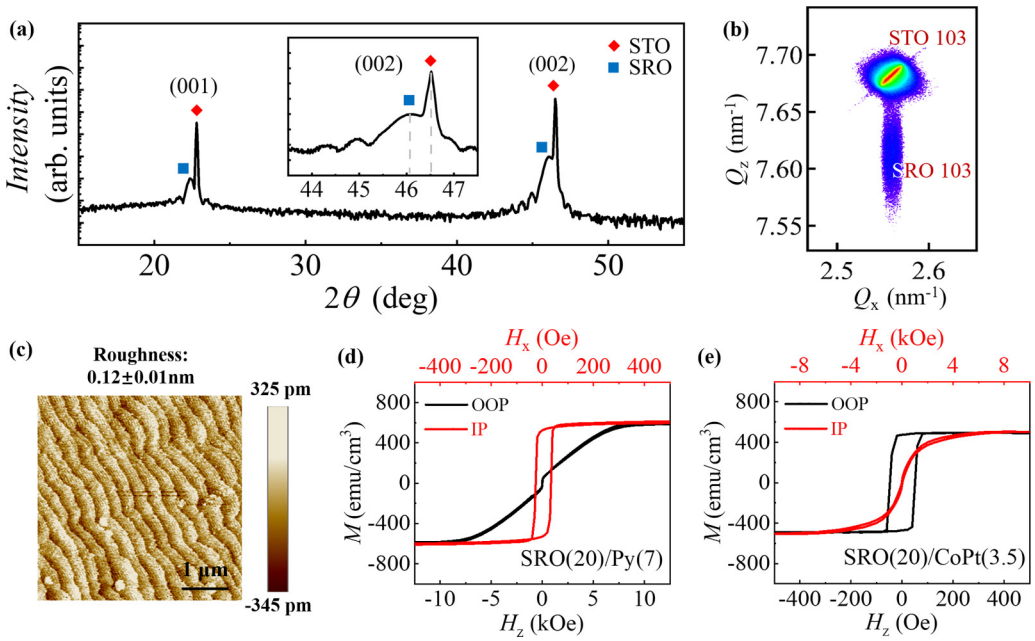

FIG. 1. SRO-based heterostructures. (a) The result of XRD θ-2θ scan for the SRO film grown on the STO (001) substrate. Inset shows the zoom-in range around (002) peaks of SRO and STO. (b) The results of reciprocal space mapping around (103) peak for the prepared film. (c) An AFM image of the SRO surface with clear terraces and a root-mean-square roughness of about 0.12 nm. (d), (e) Magnetization hysteresis loops of (d) SRO/Py and (e) SRO/CoPt measured under in-plane and perpendicular-to-plane magnetic fields (H_x and H_z), which show in-plane and perpendicular magnetic anisotropy, respectively.

Here, V_{PHE}, and V_{AHE} represent the planar Hall voltage and anomalous Hall voltage. H_{DL} and H_{FL} denote the effective field of dampinglike and fieldlike components, which correspond to $\cos\varphi$ and $\cos\varphi\cos 2\varphi$ dependencies. H_K is effective anisotropy field of Py estimated to be 6500 Oe. H_{Oe} denotes the Oersted field which has the same symmetry as H_{FL}. By fitting the measured $V_{xy}^{2\omega}$ data to Eq. (2), we obtained amplitudes of the two components varied with φ. Typical curves under $I = 3.5$ mA and $H = 1000$ Oe are shown in Fig. 2(c). Accordingly, as shown in Figs. 2(d) and 2(e), the extracted dampinglike and fieldlike voltages, V_{DL} and V_{HL}, exhibit linear dependence against $1/(H + H_K)$ and $1/H$ for I ranging

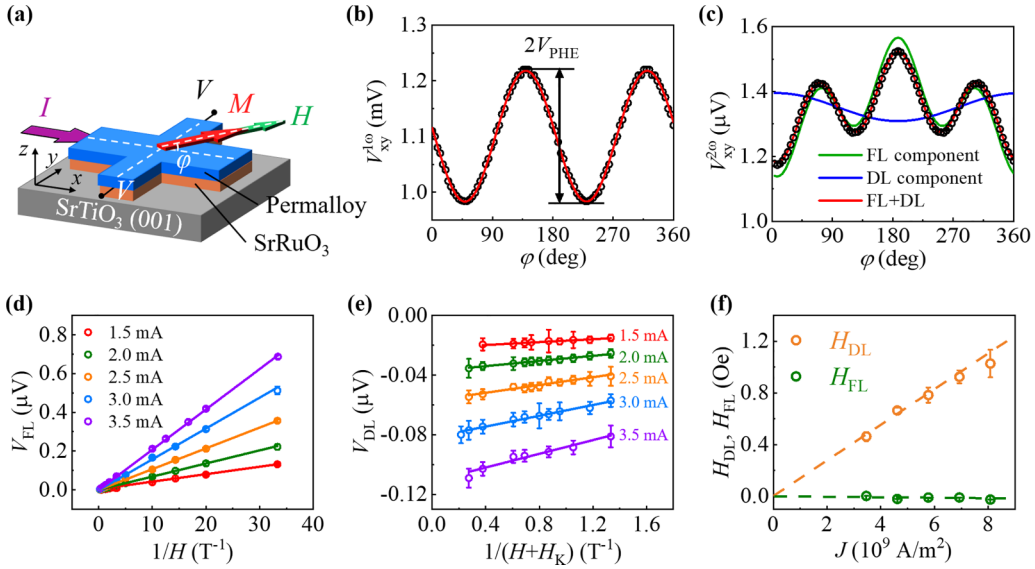

FIG. 2. Harmonic Hall voltage measurement of the SRO/Py sample. (a) A schematic diagram of the measurement for an IMA system. The current I flows along the x axis. φ is defined as the angle between I and the external magnetic field H. (b), (c) Typical first (b) and second (c) harmonic Hall voltages ($V_{xy}^{1\omega}$ and $V_{xy}^{2\omega}$) measured at $H = 1000$ Oe and $I = 3.5$ mA. The $V_{xy}^{2\omega}$ consists of the dampinglike and fieldlike components (V_{FL} and V_{DL}). (d) Linear fitting of V_{FL} against $1/H$ measured at different I. (e) Linear fitting of V_{DL} against $1/(H + H_K)$ measured at different I. (f) The equivalent fields, i.e., H_{DL} and H_{FL}, as a function of current density J.

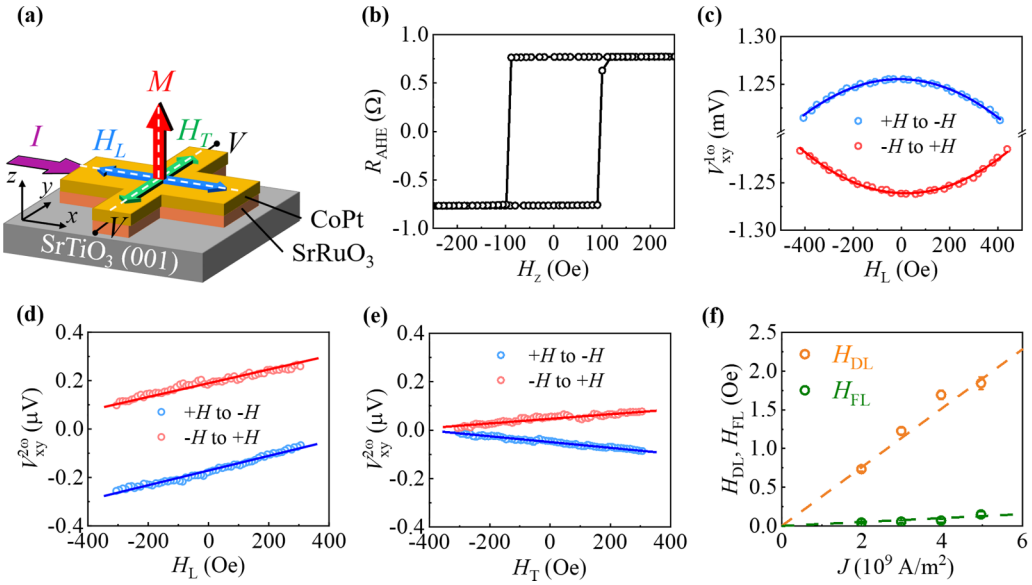

FIG. 3. Harmonic Hall voltage measurement of the SRO/CoPt sample. (a) A schematic diagram of the measurement for a PMA system. The current I flows along the x axis. The in-plane magnetic field $H_L(H_T)$ is applied along either the x (longitudinal) or y (transverse) direction. (b) The measured anomalous Hall resistance R_{AHE} as a function of out-of-plane magnetic field H_Z. The (c) first and (d) second harmonic Hall voltages acquired at $I = 3$ mA as a function of in-plane longitudinal field H_L. (e) The acquired second harmonic Hall voltage under the in-plane transverse field H_T measured at $I = 3$ mA. (f) The SOT effective fields H_{DL} and H_{FL} as a function of current density J.

1.5–3.5 mA. This indicates that our data can be well explained by Eqs. (3) and (4), thereby the H_{DL} and H_{FL} are reasonably estimated from the slopes, $V_{AHE}H_{DL}$ and $V_{PHE}(H_{FL} + H_{Oe})$, respectively. Particularly, H_{FL} is obtained by subtracting the contribution of H_{Oe}, where $H_{Oe} = \mu_0 J t_{SRO}/2$ is derived from the Biot-Savart law. Here J and t_{SRO} are current density and thickness of the SRO layer. Figure 2(f) shows the estimated effective fields as a relationship of J, where H_{DL}/J and H_{FL}/J are calculated to be 13.81 ± 0.28 Oe/(10^{11} A/m^2) and 12.32 ± 0.05 Oe/(10^{11} A/m^2). Finally, we evaluate the dampinglike (fieldlike) SOT efficiency and spin Hall conductivity via $\xi_{DL(FL)} = (2e/\hbar)(\mu_0 M_s t_{FM} H_{DL(FL)}/J)$ [19,44] and $\sigma_{SH} = \xi_{DL}\sigma_{SRO}$, where $M_S = 597$ emu/cm^3 and $t_{FM} = 7$ nm denote the saturation magnetization and thickness of the Py layer, and $\sigma_{SRO} = 64.1\times10^4$ S m^{-1} is the conductivity of the SRO layer. The evaluated values of ξ_{DL} and σ_{SH} are 0.175 and 11.2×10^4 $\hbar/2e$ S m^{-1} in the IMA system, comparable to the recent studies of SRO and the representative heavy metals, such as Pt [45–47], W [48], and Ta [49,50]. The ξ_{FL} is estimated to be -0.003, which is negligible in this system.

C. SOT efficiency of PMA system

To systematically confirm the SOT associated properties of SRO, the harmonic Hall measurements are alternatively carried out in the SRO/CoPt sample with PMA [51,52]. The measurement geometry is schematically depicted in Fig. 3(a), where the AC current I is applied along the x direction, and the magnetic easy axis of the CoPt aligns toward the z (perpendicular) direction. During the measurements, the magnetic field H is applied along either the x (longitudinal) or y (transverse) direction to estimate the effective fields H_{DL} and H_{FL} by acquiring the first and second harmonic voltages $V_{xy}^{1\omega}$ and $V_{xy}^{2\omega}$, because in the PMA configuration, the $H_{DL(FL)}$ is parallel (perpendicular) to the I in the xy plane, and can be expressed as follows:

$$H_{DL(FL)} = -2\frac{B_{DL(FL)} \pm 2\eta B_{DL(FL)}}{1 - 4\eta^2}, \tag{5}$$

$$B_{DL(FL)} = \left\{ \frac{\partial V_{xy}^{2\omega}}{\partial H} \Big/ \frac{\partial^2 V_{xy}^{1\omega}}{\partial H^2} \right\}_{H_{DL(FL)}}, \tag{6}$$

where $\eta = 0.105$ is the ratio of R_{PHE} to R_{AHE} used to exclude the contribution from the planar Hall effect. We first confirm the AHE loop of the SRO/CoPt sample, as shown in Fig. 3(b), which exhibits the typical characteristic of PMA with a sharp coercivity field of about 100 Oe. To estimate the H_{DL}, $V_{xy}^{1\omega}$ and $V_{xy}^{2\omega}$ are measured simultaneously by sweeping H along the x direction. The $V_{xy}^{1\omega}$ exhibits a characteristic parabolic behavior with opposite sign of the quadratic term for the contrary sweeping directions, while $V_{xy}^{2\omega}$ follows a linear dependence with the same sign of slopes, as shown in Figs. 3(c) and 3(d). By substituting the extracted quadratic coefficient and the slope under different J into Eqs. (5) and (6), the H_{DL} are obtained and summarized in Fig. 3(f). The H_{DL}/J_{SRO} is estimated to be 39.65 ± 1.44 Oe/(10^{11} A/m^2). Using a similar procedure while the H is applied along the y direction, the H_{FL} associated $V_{xy}^{1\omega}$ and $V_{xy}^{2\omega}$ are measured. The $V_{xy}^{2\omega}$ for H_{FL} exhibits the opposite sign of the slopes, as shown in Fig. 3(e), which is consistent with the symmetry of the fieldlike torque. Accordingly, the relationship between H_{FL} and J is plotted in Fig. 3(f), and the H_{FL}/J is estimated to be 2.42 ± 0.34Oe/(10^{11} A/m^2) after deducting the contribution of H_{Oe}. The SOT efficiency ξ_{DL}, ξ_{FL} and spin Hall conductivity σ_{SH} are evaluated to be 0.210, 0.013,

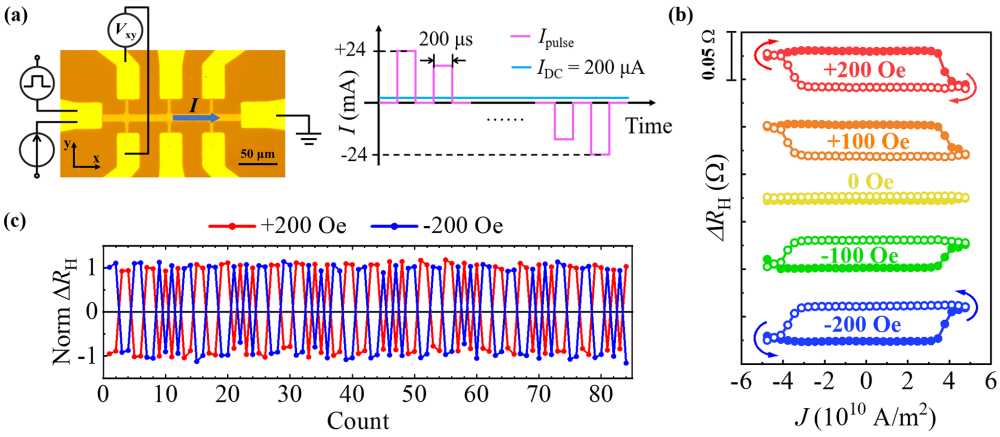

FIG. 4. Spin-orbit torque induced perpendicular magnetization switching in SRO/CoPt hybrid structure. (a) Left panel: A microscope image of the Hall bar device with electrodes together with the SOT switching measurement geometry. The pulsed current I_{pulse} and the DC constant current I_{DC} are used to switch and read the magnetization state, respectively. Right panel: the sequence diagram of I_{pulse} (±24 mA) and I_{DC} (200 μA). (b) Magnetization switching driven by I_{pulse} under various external magnetic field H_x. ΔR_H represents the change of Hall resistance. (c) SOT-induced magnetization switching measured for a train of I_{pulse} (±22 mA, 200 μs) under a field H_x of ±200 Oe.

and 4.68×10^4 $\hbar/2e$ S m^{-1} in the PMA system with M_s of 499 emu/cm^3.

D. SOT-induced magnetization switching

To directly demonstrate practical capability of the SOT that arises from SRO, we further perform current-induced magnetization switching in the SRO/CoPt sample. The measurement configuration is shown in Fig. 4(a). A train of 200-μs pulsed currents I_{pulse} with gradually increasing magnitude in the range ±24 mA is applied to trigger the magnetization switching. Concurrently, the Hall resistance is acquired under a small DC current I_{DC} of 200 μA that causes negligible influence on the magnetization state. As shown in Fig. 4(b), we observe typical SOT-induced behaviors in the PMA system. First, no switching is detected under a zero bias field due to the mirror symmetry of SOT with respect to normal plane. After applying in-plane bias fields H_x to break the symmetry, deterministic switching occurs at approximately ±19 mA. Further reversing the polarity of H_x, the chirality of the loops changes accordingly. These behaviors indicate that the current-induced switching is governed by SOT, while the Joule heating plays a minor effect (see details in Supplemental Material S2 [38]). The magnitude of the Hall resistance ΔR_H is partial with that of the AHE curve in Fig. 3(b), likely because the nonuniform pinning hampers further domain wall displacement in this domain-wall-mediated switching regime. The threshold current density J_{th} of SRO is estimated to be 3.8×10^{10} A/m^2, which is comparable to that of other novel SOT materials [8,19,53,54], and about one order of magnitude smaller than those in typical heavy metals [4,46–48,50]. Additionally, to confirm the repeatability and stability of SOT switching using SRO, multiple I_{pulse} with alternative magnitudes of ±22 mA and width of 200 μs are applied to the sample at H_x = ±200 Oe. Figure 4(c) shows the switching results of a total of 168 pulses, which exhibit a highly reproducible SOT-driven response with an almost unchanged ΔR_H, demonstrating the robustness of SRO for current-induced magnetization switching.

IV. DISCUSSION

Although previous works have demonstrated that SRO holds novel and highly tunable spin Hall properties, there is uncertain magnitude among the reported SOT efficiency in the IMA system by different measurement techniques. For a reasonable benchmark, we characterize the SOT properties of high-quality SRO in heterostructures with both IMA and PMA configuration. Since SOT characterization by ST-FMR technique in the previous studies suffers from two main issues of impedance mismatch and phase asynchrony that may introduce undesirable artifacts in the estimated results, we use a harmonic Hall voltage technique that can avoid these issues and obtain reasonable results after excluding the extrinsic factors caused from thermal effects and magnetic moment misalignment. As the results listed in Table I show, a consistent magnitude of SOT efficiency is evaluated to be 0.2 from both systems, indicating that SRO possesses the pronounced charge-spin conversion efficiency. The subsequently calculated spin Hall conductivity $\sigma_{SH} = \xi_{DL}\sigma_{SRO}$ with a value as high as 4.7×10^4 $\hbar/2e$ S m^{-1} is in agreement with that of the previous reported magnitude [14]. Moreover, we demonstrate that SOT-driven magnetization switching can be efficiently realized by SRO at room temperature. The threshold current density J_{th} is about 3.8×10^{10} A/m^2 in a pulsed time of 200 μs, taking a crucial step for utilizing SRO towards practical SOT applications.

Finally, we compare the SOT properties of SRO with other HMs. As a massively explored system, magnetic alloys combined with HMs is practically important for realizing a SOT device with the advantages of high melting point and nontoxicity. Our study clearly shows that, as listed in Table I, SRO holds comparable ξ_{DL} and σ, and about one of magnitude smaller J_{th} than that of the typical HMs. Besides, SRO also possesses excellent thermal and chemical stabilities [32], and thereby maintains low element diffusivity with the adjacent magnetic alloy layer. Such elemental diffusion should bring an adverse impact to SOT efficiency and/or magnetic properties near the heterostructure interface, hindering performance

TABLE I. Comparison of the SOT efficiency and spin Hall conductivity in different systems. $\xi_{DL(FL)}$ is the dampinglike (fieldlike) SOT efficiency, ρ_{SOC} is the resistivity of SOC layer, σ_{SH} and J_{th} present the spin Hall conductivity and threshold current density, respectively.

Sample	Magnetic anisotropy	Technique	ξ_{DL}	ξ_{FL}	ρ_{SOC} ($\mu\Omega$ cm)	σ_{SH} ($\times 10^4\ \hbar/2e^{-1}$) (S m^{-1})	J_{th} ($\times 10^{10}$) (A/m^2)	Reference
SRO(20)/Py(7)	IMA	harmonic	0.18	0.003	156	11		this work
SRO(20)/CoPt(3.5)	PMA	harmonic	0.21	0.013	450	4.7	3.8	this work
SRO(20)/Py(4) on STO(001)	IMA	ST-FMR	0.14		120	23		[15]
SRO(20)/Py(4) on STO(001)	IMA	harmonic	0.035		120	5.8		[15]
SRO(6)/Py(6) on STO(001)	IMA	ST-FMR	0.49		810	5.7		[16]
Pt(6)/Py(4)	IMA	ST-FMR	0.056		20	28		[45]
Pt(3)/Co(0.6)	PMA	harmonic	0.16		36	44	82	[46]
Pt(4)/Co(0.85)	PMA	harmonic	0.2	−0.05	50	40	32	[47]
W(6)/CoFeB(5) (β phase)	IMA	ST-FMR	0.3		170	17	18	[48]
Ta(8)/CoFeB(5) (β phase)	PMA	ST-FMR	0.15		190	7.9	48	[50]
Ta(13)/Py(4) (β phase)	IMA	ST-FMR	−0.37	0.17	122	−6.6		[49]
Ta(13)/Py(4) (mixed phase)	IMA	ST-FMR	−0.52	−0.06	45	−50		[49]

stabilities of practical devices. Therefore, we suggest that by combining these advantages, SRO should be a versatile material for realizing various SOT applications in high-quality oxide-metal hybrid systems as another choice of HMs, and in all-oxide heterostructures as a standard spin source.

V. CONCLUSION

We systematically investigate the SOT associated properties of SRO via constructing SRO/magnetic alloy hybrid systems with different magnetization easy axes. One of the main aims of our work is to accurately evaluate the SOT efficiency in SRO, and make a conclusive comparison with heavy metals. Using a harmonic Hall voltage technique in IMA and PMA configurations, we clearly demonstrate that SRO possesses a large dampinglike efficiency ξ_{DL} of about 0.2 at room temperature regardless of the magnetic alloys, which is comparable to the typical HMs. The other aim is to demonstrate the current-induced magnetization switching by SRO. We unambiguously observe the SOT-driven magnetization switching behavior, with threshold current density of 3.8×10^{10} A/m^2, which is about one magnitude smaller than that of the HMs. From these benchmarks, we suggest that transition metal oxide SRO may bring more diverse choices for SOT applications by utilizing hybrid-oxide/metal and all-oxide systems.

ACKNOWLEDGMENTS

This work was supported by the National Key Research and Development Program of China (Grants No. 2019YFA0307800 and No. 2017YFA0303600), the National Natural Science Foundation of China (Grants No. 12174406, No. 11874367, and No. 51931011), the Key Research Program of Frontier Sciences, Chinese Academy of Sciences (Grant No. ZDBS-LY-SLH008), the K.C. Wong Education Foundation (Grant No. GJTD-2020-11), the Ningbo Key Scientific and Technological Project (Grant No. 2022Z094), the Natural Science Foundation of Zhejiang Province of China (Grant No. LR20A040001), and the Beijing National Laboratory for Condensed Matter Physics.

[1] T. Seki, Y. Hasegawa, S. Mitani, S. Takahashi, H. Imamura, S. Maekawa, J. Nitta, and K. Takanashi, Giant spin Hall effect in perpendicularly spin-polarized FePt/Au devices, Nat. Mater. **7**, 125 (2008).

[2] I. M. Miron, K. Garello, G. Gaudin, P. J. Zermatten, M. V. Costache, S. Auffret, S. Bandiera, B. Rodmacq, A. Schuhl, and P. Gambardella, Perpendicular switching of a single ferromagnetic layer induced by in-plane current injection, Nature (London) **476**, 189 (2011).

[3] L. Liu, C. F. Pai, D. C. Ralph, and R. A. Buhrman, Magnetic Oscillations Driven by the Spin Hall Effect in 3-Terminal Magnetic Tunnel Junction Devices, Phys. Rev. Lett. **109**, 186602 (2012).

[4] L. Zhu, D. C. Ralph, and R. A. Buhrman, Maximizing spin-orbit torque generated by the spin Hall effect of Pt, Appl. Phys. Rev. **8**, 031308 (2021).

[5] A. R. Mellnik, J. S. Lee, A. Richardella, J. L. Grab, P. J. Mintun, M. H. Fischer, A. Vaezi, A. Manchon, E. A. Kim, N. Samarth *et al.*, Spin-transfer torque generated by a topological insulator, Nature (London) **511**, 449 (2014).

[6] Y. Wang, P. Deorani, K. Banerjee, N. Koirala, M. Brahlek, S. Oh, and H. Yang, Topological Surface States Originated Spin-Orbit Torques in Bi_2Se_3, Phys. Rev. Lett. **114**, 257202 (2015).

[7] M. Dc, R. Grassi, J. Y. Chen, M. Jamali, D. Reifsnyder Hickey, D. Zhang, Z. Zhao, H. Li, P. Quarterman, Y. Lv *et al.*, Room-temperature high spin-orbit torque due to quantum confinement in sputtered $Bi_xSe_{(1-x)}$ films, Nat. Mater. **17**, 800 (2018).

[8] N. H. D. Khang, Y. Ueda, and P. N. Hai, A conductive topological insulator with large spin Hall effect for ultralow power spin-orbit torque switching, Nat. Mater. **17**, 808 (2018).

[9] Q. Shao, G. Yu, Y. W. Lan, Y. Shi, M. Y. Li, C. Zheng, X. Zhu, L. J. Li, P. K. Amiri, and K. L. Wang, Strong Rashba-Edelstein

effect-induced spin-orbit torques in monolayer transition metal dichalcogenide/ferromagnet bilayers, Nano Lett. **16**, 7514 (2016).

[10] M. H. D. Guimaraes, G. M. Stiehl, D. MacNeill, N. D. Reynolds, and D. C. Ralph, Spin-orbit torques in $NbSe_2$/Permalloy bilayers, Nano Lett. **18**, 1311 (2018).

[11] P. Li, W. Wu, Y. Wen, C. Zhang, J. Zhang, S. Zhang, Z. Yu, S. A. Yang, A. Manchon, and X. X. Zhang, Spin-momentum locking and spin-orbit torques in magnetic nano-heterojunctions composed of Weyl semimetal WTe_2, Nat. Commun. **9**, 3990 (2018).

[12] F. Trier, P. Noël, J.-V. Kim, J.-P. Attané, L. Vila, and M. Bibes, Oxide spin-orbitronics: Spin–charge interconversion and topological spin textures, Nat. Rev. Mater. **7**, 258 (2021).

[13] H. Chen and D. Yi, Spin–charge conversion in transition metal oxides, APL Mater. **9**, 060908 (2021).

[14] Y. Ou, Z. Wang, C. S. Chang, H. P. Nair, H. Paik, N. Reynolds, D. C. Ralph, D. A. Muller, D. G. Schlom, and R. A. Buhrman, Exceptionally high, strongly temperature dependent, spin Hall conductivity of $SrRuO_3$, Nano Lett. **19**, 3663 (2019).

[15] J. Zhou, X. Shu, W. Lin, D. F. Shao, S. Chen, L. Liu, P. Yang, E. Y. Tsymbal, and J. Chen, Modulation of spin-orbit torque from $SrRuO_3$ by epitaxial-strain-induced octahedral rotation, Adv. Mater. **33**, 2007114 (2021).

[16] J. Wei, H. Zhong, J. Liu, X. Wang, F. Meng, H. Xu, Y. Liu, X. Luo, Q. Zhang, Y. Guang *et al.*, Enhancement of spin–orbit torque by strain engineering in $SrRuO_3$ films, Adv. Funct. Mater. **31**, 2100380 (2021).

[17] A. S. Patri, K. Hwang, H. W. Lee, and Y. B. Kim, Theory of large intrinsic spin Hall effect in iridate semimetals, Sci. Rep. **8**, 8052 (2018).

[18] T. Nan, T. J. Anderson, J. Gibbons, K. Hwang, N. Campbell, H. Zhou, Y. Q. Dong, G. Y. Kim, D. F. Shao, T. R. Paudel *et al.*, Anisotropic spin-orbit torque generation in epitaxial $SrIrO_3$ by symmetry design, Proc. Natl. Acad. Sci. USA **116**, 16186 (2019).

[19] L. Liu, Q. Qin, W. Lin, C. Li, Q. Xie, S. He, X. Shu, C. Zhou, Z. Lim, J. Yu *et al.*, Current-induced magnetization switching in all-oxide heterostructures, Nat. Nanotechnol. **14**, 939 (2019).

[20] A. S. Everhardt, M. Dc, X. Huang, S. Sayed, T. A. Gosavi, Y. Tang, C.-C. Lin, S. Manipatruni, I. A. Young, S. Datta *et al.*, Tunable charge to spin conversion in strontium iridate thin films, Phys. Rev. Mater. **3**, 051201(R) (2019).

[21] H. Wang, K.-Y. Meng, P. Zhang, J. T. Hou, J. Finley, J. Han, F. Yang, and L. Liu, Large spin-orbit torque observed in epitaxial $SrIrO_3$ thin films, Appl. Phys. Lett. **114**, 232406 (2019).

[22] X. Huang, S. Sayed, J. Mittelstaedt, S. Susarla, S. Karimeddiny, L. Caretta, H. Zhang, V. A. Stoica, T. Gosavi, F. Mahfouzi *et al.*, Novel spin-orbit torque generation at room temperature in an all-oxide epitaxial $La_{0.7}Sr_{0.3}MnO_3/SrIrO_3$ system, Adv. Mater. **33**, 2008269 (2021).

[23] K. Ueda, N. Moriuchi, K. Fukushima, T. Kida, M. Hagiwara, and J. Matsuno, Stacking-Order Effect on Spin-Orbit Torque, Spin Hall Magnetoresistance, and Magnetic Anisotropy in $Ni_{81}Fe_{19}$–IrO_2 Bilayers, Phys. Rev. Appl. **16**, 034039 (2021).

[24] E. Lesne, Y. Fu, S. Oyarzun, J. C. Rojas-Sanchez, D. C. Vaz, H. Naganuma, G. Sicoli, J. P. Attane, M. Jamet, E. Jacquet *et al.*, Highly efficient and tunable spin-to-charge conversion through Rashba coupling at oxide interfaces, Nat. Mater. **15**, 1261 (2016).

[25] Y. Wang, R. Ramaswamy, M. Motapothula, K. Narayanapillai, D. Zhu, J. Yu, T. Venkatesan, and H. Yang, Room-temperature giant charge-to-spin conversion at the $SrTiO_3$-$LaAlO_3$ oxide interface, Nano Lett. **17**, 7659 (2017).

[26] A. Bhattacharya and S. J. May, Magnetic oxide heterostructures, Annu. Rev. Mater. Sci. **44**, 65 (2014).

[27] Y. Tokura, M. Kawasaki, and N. Nagaosa, Emergent functions of quantum materials, Nat. Phys. **13**, 1056 (2017).

[28] K. Takiguchi, Y. K. Wakabayashi, H. Irie, Y. Krockenberger, T. Otsuka, H. Sawada, S. A. Nikolaev, H. Das, M. Tanaka, Y. Taniyasu *et al.*, Quantum transport evidence of Weyl fermions in an epitaxial ferromagnetic oxide, Nat. Commun. **11**, 4969 (2020).

[29] E. Dagotto, Complexity in strongly correlated electronic systems, Science **309**, 257 (2005).

[30] C. Ahn, A. Cavalleri, A. Georges, S. Ismail-Beigi, A. J. Millis, and J. M. Triscone, Designing and controlling the properties of transition metal oxide quantum materials, Nat. Mater. **20**, 1462 (2021).

[31] C. B. Eom, R. J. Cava, R. M. Fleming, J. M. Phillips, R. B. vanDover, J. H. Marshall, J. W. P. Hsu, J. J. Krajewski, and W. F. Peck, Single-crystal epitaxial thin films of the isotropic metallic oxides $Sr_{1-x}Ca_xRu\ O_3 (0 \leqslant x \leqslant 1)$, Science **258**, 1766 (1992).

[32] G. Koster, L. Klein, W. Siemons, G. Rijnders, J. S. Dodge, C.-B. Eom, D. H. A. Blank, and M. R. Beasley, Structure, physical properties, and applications of $SrRuO_3$ thin films, Rev. Mod. Phys. **84**, 253 (2012).

[33] S. C. Gausepohl, M. Lee, L. Antognazza, and K. Char, Magnetoresistance probe of spatial current variations in high-Tc $YBa_2Cu_3O_7$–$SrRuO_3$–$YBa_2Cu_3O_7$ Josephson junctions, Appl. Phys. Lett. **67**, 1313 (1995).

[34] H. Boschker, T. Harada, T. Asaba, R. Ashoori, A. V. Boris, H. Hilgenkamp, C. R. Hughes, M. E. Holtz, L. Li, D. A. Muller *et al.*, Ferromagnetism and Conductivity in Atomically Thin $SrRuO_3$, Phys. Rev. X **9**, 011027 (2019).

[35] Y. Gu, Q. Wang, W. Hu, W. Liu, Z. Zhang, F. Pan, and C. Song, An overview of $SrRuO_3$-based heterostructures for spintronic and topological phenomena, J. Phys. D: Appl. Phys. **55**, 233001 (2022).

[36] S. Itoh, Y. Endoh, T. Yokoo, S. Ibuka, J. G. Park, Y. Kaneko, K. S. Takahashi, Y. Tokura, and N. Nagaosa, Weyl fermions and spin dynamics of metallic ferromagnet $SrRuO_3$, Nat. Commun. **7**, 11788 (2016).

[37] W. Lin, L. Liu, Q. Liu, L. Li, X. Shu, C. Li, Q. Xie, P. Jiang, X. Zheng, R. Guo *et al.*, Electric field control of the magnetic weyl fermion in an epitaxial $SrRuO_3$ (111) thin film, Adv. Mater. **33**, 2101316 (2021).

[38] See Supplemental Material at http://link.aps.org/supplemental/10.1103/PhysRevMaterials.7.024418 for additional characterization and analysis.

[39] C. O. Avci, K. Garello, M. Gabureac, A. Ghosh, A. Fuhrer, S. F. Alvarado, and P. Gambardella, Interplay of spin-orbit torque and thermoelectric effects in ferromagnet/normal-metal bilayers, Phys. Rev. B **90**, 224427 (2014).

[40] M. Hayashi, J. Kim, M. Yamanouchi, and H. Ohno, Quantitative characterization of the spin-orbit torque using harmonic Hall voltage measurements, Phys. Rev. B **89**, 144425 (2014).

[41] J. C. Slonczewski, Current-driven excitation of magnetic multilayers, J. Magn. Magn. Mater. **159**, L1 (1996).

[42] L. Berger, Emission of spin waves by a magnetic multilayer traversed by a current, Phys. Rev. B **54**, 9353 (1996).

[43] S. Zhang, P. M. Levy, and A. Fert, Mechanisms of Spin-Polarized Current-Driven Magnetization Switching, Phys. Rev. Lett. **88**, 236601 (2002).

[44] L. Liu, O. J. Lee, T. J. Gudmundsen, D. C. Ralph, and R. A. Buhrman, Current-Induced Switching of Perpendicularly Magnetized Magnetic Layers using Spin Torque from the Spin Hall Effect, Phys. Rev. Lett. **109**, 096602 (2012).

[45] L. Liu, T. Moriyama, D. C. Ralph, and R. A. Buhrman, Spin-Torque Ferromagnetic Resonance Induced by the Spin Hall Effect, Phys. Rev. Lett. **106**, 036601 (2011).

[46] K. Garello, I. M. Miron, C. O. Avci, F. Freimuth, Y. Mokrousov, S. Blugel, S. Auffret, O. Boulle, G. Gaudin, and P. Gambardella, Symmetry and magnitude of spin-orbit torques in ferromagnetic heterostructures, Nat. Nanotechnol. **8**, 587 (2013).

[47] L. Zhu, D. C. Ralph, and R. A. Buhrman, Spin-Orbit Torques in Heavy-Metal-Ferromagnet Bilayers with Varying Strengths of Interfacial Spin-Orbit Coupling, Phys. Rev. Lett. **122**, 077201 (2019).

[48] C.-F. Pai, L. Liu, Y. Li, H. W. Tseng, D. C. Ralph, and R. A. Buhrman, Spin transfer torque devices utilizing the giant spin Hall effect of tungsten, Appl. Phys. Lett. **101**, 122404 (2012).

[49] A. Kumar, R. Sharma, K. I. Ali Khan, C. Murapaka, G. J. Lim, W. S. Lew, S. Chaudhary, and P. K. Muduli, Large damping-like spin–orbit torque and improved device performance utilizing mixed-phase Ta, ACS Appl. Electron. Mater. **3**, 3139 (2021).

[50] L. Liu, C.-F. Pai, Y. Li, H. W. Tseng, D. C. Ralph, and R. A. Buhrman, Spin-torque switching with the giant spin Hall effect of tantalum, Science **336**, 555 (2012).

[51] S. Emori, U. Bauer, S. M. Ahn, E. Martinez, and G. S. Beach, Current-driven dynamics of chiral ferromagnetic domain walls, Nat. Mater. **12**, 611 (2013).

[52] J. Kim, J. Sinha, M. Hayashi, M. Yamanouchi, S. Fukami, T. Suzuki, S. Mitani, and H. Ohno, Layer thickness dependence of the current-induced effective field vector in Ta|CoFeB|MgO, Nat. Mater. **12**, 240 (2013).

[53] J. Ding, C. Liu, V. Kalappattil, Y. Zhang, O. Mosendz, U. Erugu, R. Yu, J. Tian, A. DeMann, S. B. Field *et al.*, Switching of a magnet by spin-orbit torque from a topological Dirac semimetal, Adv. Mater. **33**, 2005909 (2021).

[54] P. Li, J. Kally, S. S.-L. Zhang, T. Pillsbury, J. Ding, G. Csaba, J. Ding, J. S. Jiang, Y. Liu, R. Sinclair *et al.*, Magnetization switching using topological surface states, Sci. Adv. **5**, eaaw3415 (2019).